PROCEEDINGS OF SPIE

SPIEDigitalLibrary.org/conference-proceedings-of-spie

Pulsed dynamics in a system of coupled silicon photonic crystal cavity-waveguide nanostructures

Fernandez Laguna, Victor Manuel, Ren, Qun, Panoiu, Nicolae

Victor Manuel Fernandez Laguna, Qun Ren, Nicolae C. Panoiu, "Pulsed dynamics in a system of coupled silicon photonic crystal cavity-waveguide nanostructures," Proc. SPIE 11081, Active Photonic Platforms XI, 110812D (5 September 2019); doi: 10.1117/12.2526658

SPIE.

Event: SPIE Nanoscience + Engineering, 2019, San Diego, California, United States

Pulsed dynamics in a system of coupled silicon photonic crystal cavity-waveguide nanostructures

Victor M. Fernandez Laguna[a,b], Qun Ren[b], and Nicolae C. Panoiu[b]

[a]Airbus Defence and Space, Gunnels Wood Road, Stevenage SG1 2AS, United Kingdom
[b]Department of Electronic and Electrical Engineering, University College London, Torrington Place, London WC1E 7JE, United Kingdom

ABSTRACT

Pulsed dynamics are rigorously studied in coupled silicon photonic crystal cavity-waveguide nanostructures by developing a computational model based on coupled-mode theory, which describes cavity-waveguide coupling effects, key nonlinear interactions, such as the Kerr effect, two-photon-absorption, free-carrier (FC) dispersion and FC absorption, as well as waveguide dispersion effects. Propagation of optical pulses in a photonic system consisting of two photonic crystal cavities coupled to a photonic crystal waveguide operating in the slow-light regime is analyzed. Moreover, the influence of different parameters on pulse dynamics is investigated, including the separation between cavities, the distance between the cavities and the waveguide, and the input pulse width.

Keywords: Silicon, photonic crystals cavities, photonic crystals waveguides, Kerr effect, slow-light, coupled-mode theory, optical filters

1. INTRODUCTION

The recent growth in networks-on-chip (NoC) applications has been somewhat limited by several important disadvantages the electrical interconnects have shown, such as poor bandwidth, large power dissipation at high frequencies due to track losses, need for impedance matching, and crosstalk between electrical paths.[1,2] Optical interconnects are found to be a potential solution to all of these challenges, and have an additional key advantage, namely they have a smaller footprint. However, most of the on-chip optical devices that that have been demonstrated employed III-V semiconductors, especially the active devices, making the co-integration with electronics a complicated and expensive task.

Silicon photonics is becoming one of the key enablers to bring electronic and optical domains together onto the same chip, and CMOS-compatible designs have become a reality for several applications.[3,4] In fact, silicon photonic waveguides (Si-PhWGs) are a good alternative to the III-V semiconductor devices, primarily due to the high refractive index of silicon, which allows the design of high-index contrast waveguides in which the nonlinearities are enhanced by a strong confinement of the electromagnetic field.[5] Nevertheless, Si-PhWGs lack engineering flexibility when a broad tuning of their optical properties is required by a specific application.

Photonic crystals (PhCs) can mitigate this limitation because they are defined by a larger set of parameters. They consist of a periodic pattern in a slab of material, the corresponding period being commensurate with the operating optical wavelength. Depending on how the periodic dielectric medium is defined, the device could be used for multiple purposes, from the design of ultra-small, narrow-band filters[6,7] to omnidirectional mirrors, waveguide bends, and highly dispersive, active diffractive elements.[8–12] In particular, this is possible thanks to the wide tuning of the group-velocity (GV) v_g of the propagating modes that PhCs allow. Especially remarkable is the slow-light regime, where light-matter interaction is enhanced and both the linear and non-linear optical effects become substantially important.[13–17] Interesting applications have emerged around the control of optical properties via slow-light tuning, such as optical buffering or time domain processing of optical signals.[18–20]

In this paper, we introduce a comprehensive and rigorous theoretical model describing pulse propagation in coupled silicon PhCl cavity-waveguide nanostructures, along with its computational implementation. The

Further author information:
V.M.F.L.: E-mail: victor.laguna.15@ucl.ac.uk

Active Photonic Platforms XI, edited by Ganapathi S. Subramania, Stavroula Foteinopoulou,
Proc. of SPIE Vol. 11081, 110812D · © 2019 SPIE · CCC code: 0277-786X/19/$21
doi: 10.1117/12.2526658

mathematical model, which is described in section 2, is based on the coupled-mode theory and takes into account the cavity-waveguide coupling effects, key linear and nonlinear interactions, such as waveguide dispersion effects, free-carrier (FC) dispersion, and FC absorption (FCA), as well as the Kerr effect and two-photon absorption (TPA). In the same section, we also discuss how the coupled nonlinear Schrödinger equations (NLSE) describing the pulse dynamics are computationally solved using the Newton-Raphson technique for nonlinear systems of partial differential equations. Then, in section 3, we show the results of employing the theoretical model to analyze the propagation of pulses in a photonic system consisting of two interacting PhC cavities coupled to a PhC waveguide operating in the slow-light regime. In particular, we solve the pulse dynamics of forward- and backward-propagating pulses, both in time and frequency domains; the time dependence of the energy at each cavity; and the FC dynamics in the cavities and waveguide. Moreover, the influence of different system parameters, such as the separation distance between cavities, the distance between cavities and waveguide, and the width of the input pulse, is investigated, too. In particular, we illustrate how our computational tool can be employed to find the optimum separation between cavities that minimizes the amplitude of the backward-propagating pulse at the input. Finally, in section 4, we summarize the main conclusions.

2. THEORETICAL MODEL

Modelling the interaction between optical cavities and waveguides is a complex task given that the effect of placing a number of cavities alongside a waveguide not only affects the forward-propagating modes by coupling energy back and forth, but also generates backward-propagating pulses. In this section, we derive the mathematical equations required to solve the pulsed dynamics of a system with two PhC cavities placed alongside a PhC waveguide. It must be made clear that the mathematical model presented in this section can be easily applied to any number of cavities.

2.1 Photonic crystal waveguide and cavity modes

The Si-PhC structure considered in this work is a honeycomb-type periodic lattice of air holes with lattice constant, a, built within a homogeneous silicon slab of height, h. The waveguide is created by removing a row of the lattice, which produces a line defect. Cavities, though, are created by removing specific holes, which produces local defects in the periodic lattice. A simple representation of the structure is shown in Fig. 1a), where a couple of cavities are placed alongside the waveguide. The blue arrows represent the coupling between the waveguide and cavity modes, whereas the red arrow represents the coupling between cavities. The effective cavity length parameter, l_p, is also illustrated.

The corresponding photonic band structure and the waveguide modes it supports have been obtained with an electromagnetic solver, MPB,[21] which implements the plane-wave expansion (PWE) method. The calculations carried out using this tool are based on the Block theorem, namely the optical modes of the waveguide are periodic

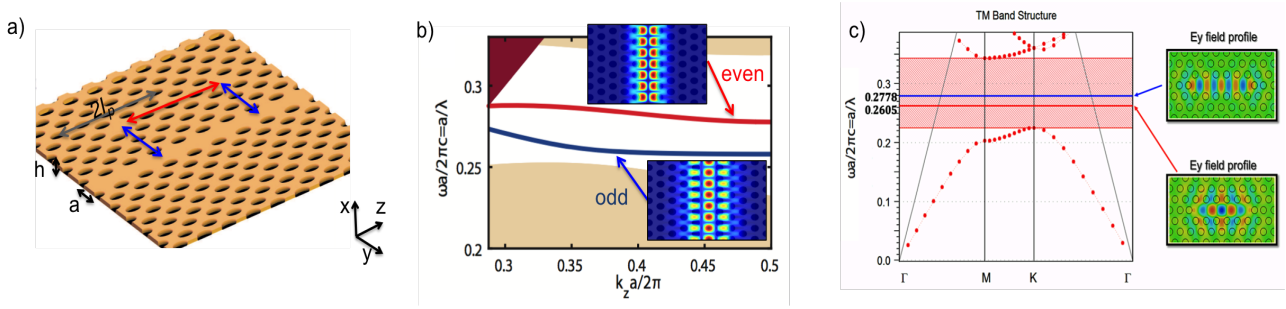

Figure 1. (a) Simplified model of the PhC structure. The blue and red arrows represent the cavity-cavity and cavity-waveguide coupling, respectively. (b) Band diagram for the isolated waveguide with a slab height of $h = 0.6a$ and radius of the holes $r = 0.29a$. The brown area corresponds to the light cone. The insets represent the field profiles of the two waveguide modes. (c) Band diagram for the isolated cavity based on same parameters as in (b). The grey lines mark the boundaries of the light cone. The insets represent the field profiles for the two optical cavity modes.

along the z-axis.[8] Consequently, the propagation constant k_z is restricted to the domain $k_z \in [-\pi/a, \pi/a]$. The structure analyzed is a supercell with dimensions $6a \times 19\sqrt{3}/2a \times a$ along the x-, y-, and z-axis, respectively, the computational grid being $a/60$, $a\sqrt{3}/120$, and $a/60$, for x, y, and z, respectively.

As presented in Fig. 1b), the waveguide has two fundamental TE-like optical guiding modes located in the band-gap of the unperturbed PhC, one y-even and the other y-odd. The index of refraction considered for the silicon slab is $n_{Si} \equiv n = 3.48$, its height $h = 0.6a$, and the radius of the holes $r = 0.29a$. The insets represent the amplitude of the normalized magnetic field H_x for the y-even and y-odd guided modes at $k_z = 0.43455$, calculated in the plane $x = 0$, for which it corresponds a group index $n_g = c/v_g = 82.37$.

Regarding the cavities studied in this paper, they are created by removing five of the holes from the original hexagonal lattice. In Fig. 1c), we show the band diagram of the cavity modes. The field profiles are obtained by employing BandSOLVE,[22] whereas the resonant frequencies and Q factors are obtained by using the finite-difference time-domain (FDTD) simulation software MEEP.[23] From the insets, it can be observed that the cavity modes are not perfectly localized, but they spread to some extent outside the cavity. Indeed, the resulting modes are resonances which couple radiation modes located in the light cone (grey lines). In order to improve the Q-factor, the design of this cavity includes a slight displacement of the holes at the edges.[24] In fact, the low frequency resonance shown in Fig. 1c) has the highest Q-factor for $a = 333\,\text{nm}$ when the holes at edges have been displaced by $0.15a$.

Unless otherwise specified, all simulation results discussed in this paper are based on a PhC slab with $a = 333\,\text{nm}$, the cavity mode at normalized frequency $a/\lambda = 0.2605$, with $Q_c = 111693$, and the slow-light mode at the same frequency, whose normalized wave vector is $k_z = 0.43455$ and group velocity is $v_g = 0.01214c$.

2.2 Mathematical model

The approach we used in our analysis contains the following steps. First, we consider an isolated waveguide to which the cavities are added as perturbations of the dielectric constant, whereas in the second step we consider the opposite case, this is, we consider an isolated cavity to which any other additional cavities and the waveguide are added as perturbations. In both cases, the mathematical derivation begins with the Maxwell equations describing each scenario, i.e. unperturbed and perturbed, which are then related by the Lorentz reciprocity theorem (for more details regarding the derivation of the mathematical model, see these references[25–27]). Subsequently, the linear and nonlinear components of the polarization term are incorporated as perturbations. Combining the results obtained at each step provides the mathematical model. In the last step, the corresponding equations are normalized to reduce the computational effort, leading to the following set of equations for the optical fields of the forward- and backward-propagating pulses as well as the optical fields of the two cavity modes, respectively:

$$
\begin{aligned}
&i\left[\frac{\partial U_+}{\partial \zeta} + \frac{a}{T_0 v_{g,+}}\frac{\partial U_+}{\partial \tau}\right] - \frac{a}{{T_0}^2}\frac{\beta_{2,+}}{2}\frac{\partial^2 U_+}{\partial \tau^2} + \frac{\Omega a}{T_0}(C_{++} + \theta^w_{++})U_+ \\
&\quad + \frac{3\Omega\epsilon_0 a P_0}{16 T_0}\left[K^w_{+,+-+}|U_+|^2 + (K^w_{+,++-} + K^w_{+,-++})|U_-|^2\right]U_+ \\
&\quad + e^{-i(\Omega_{c_1}-\Omega)\tau}\frac{\sqrt{E_0}\Omega_{c_1} a}{\sqrt{P_0}T_0}C^w_{+,c_1}U_{c_1} + ie^{-i(\Omega_{c_1}-\Omega)\tau}\frac{\sqrt{E_0}a}{\sqrt{P_0}T_0}C^c_{+,c_1}\frac{\partial U_{c_1}}{\partial \tau} \\
&\quad + e^{-i(\Omega_{c_2}-\Omega)\tau}\frac{\sqrt{E_0}\Omega_{c_2} a}{\sqrt{P_0}T_0}C^w_{+,c_2}U_{c_2} + ie^{-i(\Omega_{c_2}-\Omega)\tau}\frac{\sqrt{E_0}a}{\sqrt{P_0}T_0}C^c_{+,c_2}\frac{\partial U_{c_2}}{\partial \tau} = 0,
\end{aligned} \tag{1}
$$

$$
\begin{aligned}
&i\left[\frac{-\partial U_-}{\partial \zeta} + \frac{a}{T_0 v_{g,-}}\frac{\partial U_-}{\partial \tau}\right] - \frac{a}{{T_0}^2}\frac{\beta_{2,-}}{2}\frac{\partial^2 U_-}{\partial \tau^2} + \frac{\Omega a}{T_0}(C_{--} + \theta^w_{--})U_- \\
&\quad + \frac{3\Omega\epsilon_0 a P_0}{16 T_0}\left[K^w_{-,-+-}|U_-|^2 + (K^w_{-,--+} + K^w_{-,+--})|U_+|^2\right]U_- \\
&\quad + e^{-i(\Omega_{c_1}-\Omega)\tau}\frac{\sqrt{E_0}\Omega_{c_1} a}{\sqrt{P_0}T_0}C^w_{-,c_1}U_{c_1} + ie^{-i(\Omega_{c_1}-\Omega)\tau}\frac{\sqrt{E_0}a}{\sqrt{P_0}T_0}C^c_{-,c_1}\frac{\partial U_{c_1}}{\partial \tau} \\
&\quad + e^{-i(\Omega_{c_2}-\Omega)\tau}\frac{\sqrt{E_0}\Omega_{c_2} a}{\sqrt{P_0}T_0}C^w_{-,c_2}U_{c_2} + ie^{-i(\Omega_{c_2}-\Omega)\tau}\frac{\sqrt{E_0}a}{\sqrt{P_0}T_0}C^c_{-,c_2}\frac{\partial U_{c_2}}{\partial \tau} = 0,
\end{aligned} \tag{2}
$$

$$i\left[\frac{\partial U_{c_1}}{\partial \tau}+\frac{\Omega_{c_1}}{Q_{c_1}}U_{c_1}\right]+\Omega_{c_1}(C^{w}_{c_1,c_1}+J_{c_1,c_1})U_{c_1}+\frac{3\Omega_{c_1}\epsilon_0 E_0}{16}K^{c}_{c_1}|U_{c_1}|^2U_{c_1}$$
$$+e^{-i(\Omega-\Omega_{c_1})\tau}\frac{\sqrt{P_0}}{\sqrt{E_0}}\left[\bar{C}^{c*}_{+,c_1}(i\frac{\partial U_+}{\partial\tau}+(\Omega-\Omega_{c_1})U_+)+\bar{C}^{w*}_{+,c_1}\Omega U_+\right.$$
$$\left.+\bar{C}^{c*}_{-,c_1}(i\frac{\partial U_-}{\partial\tau}+(\Omega-\Omega_{c_1})U_-)+\bar{C}^{w*}_{-,c_1}\Omega U_-\right]=0, \tag{3}$$

$$i\left[\frac{\partial U_{c_2}}{\partial \tau}+\frac{\Omega_{c_2}}{Q_{c_2}}U_{c_2}\right]+\Omega_{c_2}(C^{w}_{c_2,c_2}+J_{c_2,c_2})U_{c_2}+\frac{3\Omega_{c_2}\epsilon_0 E_0}{16}K^{c}_{c_2}|U_{c_2}|^2U_{c_2}$$
$$+e^{-i(\Omega-\Omega_{c_2})\tau}\frac{\sqrt{P_0}}{\sqrt{E_0}}\left[\bar{C}^{c*}_{+,c_2}(i\frac{\partial U_+}{\partial\tau}+(\Omega-\Omega_{c_2})U_+)\right.$$
$$\left.+\bar{C}^{w*}_{+,c_2}\Omega U_++\bar{C}^{c*}_{-,c_2}(i\frac{\partial U_-}{\partial\tau}+(\Omega-\Omega_{c_2})U_-)+\bar{C}^{w*}_{-,c_2}\Omega U_-\right]=0, \tag{4}$$

where $\zeta=z/a$ and $\tau=t/T_0$ are the normalized distance and time, respectively, with T_0 being the width of the input pulse, U_+, U_-, and U_{c_1/c_2} represent the normalized complex amplitudes of the forward-propagating and backward-propagating waveguide modes and the two cavity modes, $\Omega=\omega T_0$, P_0 the input pulse peak power, E_0 the characteristic cavity energy, $\beta_{2,\pm}$ the GVD parameter of the waveguide modes, $v_{g,\pm}$ the group-velocities of the waveguide modes, and Ω_{c_p} and Q_{c_p} the resonance frequency and Q-factor of the cavity p, respectively. In addition, the coupling coefficients are defined as follows:

$$C_{++}=\frac{a}{4W_+v_{g,+}}\int_S(\epsilon^d_{c_1}\mathbf{e}^*_+\cdot\mathbf{e}_++\epsilon^d_{c_2}\mathbf{e}^*_+\cdot\mathbf{e}_+)dS, \tag{5}$$

$$C_{--}=\frac{a}{4W_-v_{g,-}}\int_S(\epsilon^d_{c_1}\mathbf{e}^*_-\cdot\mathbf{e}_-+\epsilon^d_{c_2}\mathbf{e}^*_-\cdot\mathbf{e}_-)dS, \tag{6}$$

$$\theta^w_{++}=\frac{a}{4v_{g,+}W_+}\int_S(\delta\epsilon^w_{FC}+\delta\epsilon_{\text{loss}})\cdot\mathbf{e}^*_+\cdot\mathbf{e}_+dS, \tag{7}$$

$$\theta^w_{--}=\frac{a}{4v_{g,-}W_-}\int_S(\delta\epsilon^w_{FC}+\delta\epsilon_{\text{loss}})\cdot\mathbf{e}^*_-\cdot\mathbf{e}_-dS, \tag{8}$$

$$C^w_{\alpha,c_p}=\frac{\sqrt{a}e^{-i\beta_\alpha z}}{4\sqrt{v_{g,\alpha}W_\alpha W_{c_p}}}\int_S\epsilon^d_w\mathbf{e}^*_\alpha\cdot\mathbf{e}_{c_p}dS, \tag{9}$$

$$C^c_{\alpha,c_p}=\frac{\sqrt{a}e^{-i\beta_\alpha z}}{4\sqrt{v_{g,\alpha}W_\alpha W_{c_p}}}\int_S(\mu\mathbf{h}^*_\alpha\cdot\mathbf{h}_{c_p}+\epsilon_{c_p}\mathbf{e}^*_\alpha\cdot\mathbf{e}_{c_p})dS, \tag{10}$$

$$K^w_{\alpha,\alpha_1\alpha_2\alpha_3}=a^2\frac{e^{i(\alpha_1+\alpha_2+\alpha_3-\alpha)\beta_\alpha z}}{v^2_{g,\alpha}W^2_\alpha}\int_S\mathbf{e}^*_\alpha\cdot\hat{\chi}^{(3)}\vdots\mathbf{e}_{\alpha_1}\mathbf{e}_{\alpha_2}\mathbf{e}_{\alpha_3}dS, \tag{11}$$

$$C^w_{c_pc_p}=\frac{1}{4W_{c_p}}\int_{V_{c_p}}\epsilon^d_w\mathbf{e}^*_{c_p}\cdot\mathbf{e}_{c_p}dV, \tag{12}$$

$$J_{c_pc_p}=\frac{1}{4W_{c_p}}\int_{V_{c_p}}\delta\epsilon_{FC,c_p}\mathbf{e}_{c_p}\cdot\mathbf{e}^*_{c_p}dV, \tag{13}$$

$$K^c_{c_p}=\frac{1}{W^2_{c_p}}\int_{V_{c_p}}\mathbf{e}^*_{c_p}\cdot\hat{\chi}^{(3)}\vdots\mathbf{e}_{c_p}\mathbf{e}^*_{c_p}\mathbf{e}_{c_p}dV, \tag{14}$$

$$C^{c*}_{\alpha,c_p}=\frac{\sqrt{a}e^{i\beta_\alpha z}}{4\sqrt{v_{g,\alpha}W_\alpha W_{c_p}}}\int_S(\mu\mathbf{h}_\alpha\cdot\mathbf{h}^*_{c_p}+\epsilon_{c_p}\mathbf{e}_\alpha\cdot\mathbf{e}^*_p)dS, \tag{15}$$

$$C^{w*}_{\alpha,c_p}=\frac{\sqrt{a}e^{i\beta_\alpha z}}{4\sqrt{v_{g,\alpha}W_\alpha W_{c_p}}}\int_S\epsilon^d_w\mathbf{e}_\alpha\cdot\mathbf{e}^*_{c_p}dS, \tag{16}$$

with $\alpha, \alpha_1, \alpha_2, \alpha_3$ taking the values of $+$ or $-$, which represents forwards and backwards propagation, respectively, and $p = 1, 2$ indexes the cavity number. In addition, $\mathbf{e}$ and $\mathbf{h}$ are the electric and magnetic fields of the corresponding optical mode, respectively, $W_{\pm}$ is the energy carried by the waveguide modes, W_{c_p} the energy within the cavity p, $\epsilon^d_{c_p}$ is the dielectric function that adds the cavity p as a defect to the ideal isolated waveguide, $\delta\epsilon^w_{FC}$ is the refractive index change on the waveguide due to FCs, $\delta\epsilon_{\text{loss}}$ models the propagation loss of the waveguide, ϵ^d_w is the dielectric function that adds the waveguide as a defect to the ideal isolated cavity, ϵ_{c_p} is the unperturbed dielectric function for the cavity p, $\hat{\chi}^3$ is the third-order susceptibility tensor of silicon and, finally, $\delta\epsilon_{FC,c_p}$ is the refractive index change on the cavity p due to FCs. It must be noted that the barred coupling coefficients in the cavity equations are calculated by taking the integral over the length parameter l_p along the z-direction around each cavity.

In the next step of our analysis we derive the equations describing the FD dynamics in the waveguide and cavities. In order to derive these equations, we impose that condition that the optical energy lost via TPA is equal to the energy of the generated FCs; the details of this procedure can be found elsewhere.[25–27] In the case of the waveguide, the result of this procedure is applied to both the backward- and forward-propagating modes, the total FC density being the sum of the FC density corresponding to the two modes, $N = N_+ + N_-$. equations and they are combined together. Finally, we introduce the normalized functions and parameters, $\bar{N} = N/N_0$, $\bar{N}_{c_p} = N_{c_p}/N_0$, $\bar{A}_{nl,w} = A_{nl,w}/a^2$, and $\bar{V}_{nl,c_p} = V_{nl,c_p}/a^3$, where N_0 is a characteristic FC density, and $A_{nl,w}$ and V_{nl,c_p} are the effective transverse area of the waveguide and effective volume of the cavity p, respectively. The resulting normalized equations for the FC dynamics are:

$$\frac{\partial \bar{N}}{\partial \tau} = -\frac{T_0 \bar{N}}{\tau_c} + \frac{3\epsilon_0 T_0 P_0^2}{32\hbar \bar{A}_{nl,w} a^2 N_0}\Big\{K^{w\prime\prime}_{+,+-+}|U_+|^4 + (K^{w\prime\prime}_{+,++-} + K^{w\prime\prime}_{+,-++})|U_+|^2|U_-|^2 + K^{w\prime\prime}_{-,-+-}|U_-|^4 + (K^{w\prime\prime}_{-,--+} + K^{w\prime\prime}_{+,+--})|U_+|^2|U_-|^2\Big\}, \tag{17}$$

$$\frac{\partial \bar{N}_{c_1}}{\partial \tau} = -\frac{T_0 \bar{N}_{c_1}}{\tau_c} + \frac{3\epsilon_0 T_0 E_0^2}{32\hbar \bar{V}_{nl,c_1} a^3 N_0} K^{c\prime\prime}_{c_1}|U_{c_1}|^4, \tag{18}$$

$$\frac{\partial \bar{N}_{c_2}}{\partial \tau} = -\frac{T_0 \bar{N}_{c_2}}{\tau_c} + \frac{3\epsilon_0 T_0 E_0^2}{32\hbar \bar{V}_{nl,c_2} a^3 N_0} K^{c\prime\prime}_{c_2}|U_{c_2}|^4, \tag{19}$$

where $\tau_c \approx 500\,\text{ps}$ is the FC recombination time in silicon[28] and the symbol "$\prime\prime$" refers to the imaginary part of a complex number. Note that degenerate and non-degenerate TPA effects are implicit in Eq. (17) via the imaginary parts of the nonlinear susceptibilities.[29] In addition, the effective transverse area of the region in which FCs are generated has been assumed to be the waveguide transverse area $A_{nl,w} = ah$, whereas the nonlinear volume of the cavity was assumed to be the volume of a rectangular three-dimensional box in which the cavity field is contained. Moreover, N_0 is chosen to be the FC density that leads to a change of the refractive index of silicon $\delta n_{FC} = 0.01$, as per Drude model. Finally, E_0 is calculated by imposing steady-state conditions ($\frac{\partial \bar{N}_{c_p}}{\partial \tau} = 0$) in Eq. (18) or Eq. (19) and requiring that $|U_{c_p}| = 1$ and $N_{c_p} = N_0$, $p = 1, 2$.

2.3 Computational method

In order to determine computationally the unknown functions, namely $U_+(\zeta, \tau)$, $U_-(\zeta, \tau)$, $\bar{N}(\zeta, \tau)$, $U_{c_p}(\tau)$, and $\bar{N}_{c_p}(\tau)$, $p = 1, 2$, one must discretize them on a computational domain and use proper boundary conditions. The first step consists of discretizing the independent variables, therefore the ζ dimension is divided in P points and τ dimension is similarly divided in M points. Consequently, the spatial and temporal resolutions are:

$$\Delta\zeta = \frac{L_{sim}}{aP}, \tag{20}$$

$$\Delta\tau = \frac{T_{sim}}{T_0 M}, \tag{21}$$

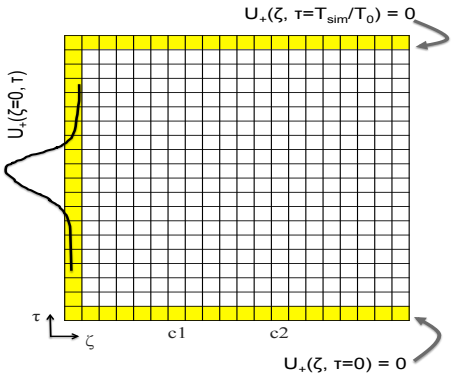

Figure 2. Schematics of discretization matrix and boundary conditions for the forward-propagating mode equation.

with L_{sim} the simulation distance and T_{sim} the simulation time.

The result of this discretization approach is a $P \times M$ matrix that represents the temporal dynamics of each unknown at each longitudinal step. Using this matrix, the boundary conditions that apply for each of the unknowns can be set. In Fig. 2 we illustrate the case of the equation for the forward-propagating mode. The labels "c_1" and "c_2" indicate the location of the two cavities, whereas the white area represents the unknown values for the forward-propagating mode. Considering the boundary conditions in the spatial dimension, the derivatives are discretized using the backward-difference formula.

Figure 2 illustrates some physical conditions employed in our computations. First, the simulation time T_{sim} must be long enough to ensure that the power carried by the forward-propagating mode at the end-facet of the waveguide is negligible. Thus, one should take into account not only the input pulse width and the time the forward mode takes to propagate to the end-facet of the simulated waveguide, but also the time delay added by the cavities when energy is coupled back to the waveguide modes. At $\zeta = 0$, we assume that the input pulse is not distorted by the backwards propagating mode. This will obviously apply only when the pulse width is smaller than the time it would take the forward-propagating mode to arrive at the first cavity c_1 and for the energy coupled to the backward-propagating mode to arrive to $\zeta = 0$. This condition can always be fulfilled by extending the simulation distance as necessary.

Regarding now the backward-propagating mode described by Eq. (2), we assume that the power it carries is zero at both edges of the time domain. This means that the simulation time must be generally longer than the time it takes for the last amount of energy coupled from cavity c_2 to the backward mode to propagate until the beginning of the waveguide. Another important point here is that we assume that there is no backward-propagating mode beyond the cavity c_2, i.e. there is no reflection at the end-facet of the waveguide. Under these conditions, the derivative is discretized using the forward finite-difference scheme.

In the case of the dynamics of the fields in the two cavities, described by Eqs. (3) and (4), the numerical implementation is simpler since we are solving for functions that depend on a single variable. The discretization matrix in this case will be, in fact, a vector. Only the initial boundary condition in time is specified, set to be equal to zero, so that the backward finite-difference scheme is used.

Finally, the FCs dynamics described by Eqs. (17), (18), and (19) require a couple of additional computational matrices. Except for the initial point in time, at which we assume there are no FCs anywhere along the waveguide and the cavities, the remaining of the spatio-temporal matrix must be determined. On the other hand, the FCs in the cavities are discretized by assuming that the FC density in the cavities at $\tau = 0$ is zero and, from there, solve for both unknowns for all time points. Consequently, the backward finite-difference scheme is used to express the derivatives for the FCs in the waveguide and cavities.

The computational algorithm employs the Newton-Raphson method[30] to solve the corresponding system of nonlinear equations. It has been implemented in C++ using LAPACK libraries.[31] The algorithm requires the input of all coefficients, which have been calculated using of three computational tools: BandSOLVE and MEEP,

to calculate the mode profile and Q-factor of each cavity, respectively; MPB, to calculate the mode profile of the waveguide modes; and Matlab, to process the waveguide and cavity mode profiles and compute various coupling coefficients.

3. SIMULATION RESULTS AND DISCUSSION

In this section, we will validate our theoretical model by analyzing the pulse and FC density dynamics determined for a specific scenario and then we will use our model to study the influence of different parameters on the pulsed dynamics. In particular, we investigate the relationship between the pulse dynamics in the photonic structure and parameters such as the pulse width T_0, the separation distance between the cavities and the waveguide, d_{cw}, and the separation distance between cavities, d_{cc}. In all simulations the input and output regions have a length of $20a$. These regions ensure that the pulse dynamics are stabilized at the input and output ports.

Figure 3 shows the evolution of the forward- and backward-propagating pulses in the case when the input pulse has a temporal width of $T_0 = 10\,\text{ps}$ and peak power $P_0 = 1\,\text{mW}$. The two identical cavities are separated by $d_{cc} = 20a$ and a cavity-waveguide separation of $d_{cw} = 2.5a\sqrt{3}$, corresponding to four rows of holes between the waveguide and the cavities. This scenario is suitable to validate the theoretical model because it is the case with optimum coupling between the waveguide and the cavities, as we will demonstrate later on.

Under these conditions, the key parameter in the model which determines the Q-factor of the cavities is the coupling coefficient $C_{cc}^{w} = 2.7392 \cdot 10^{-5}$, which reduces the effective Q-factor to $Q_{e,p} \approx (\frac{1}{Q_p} + \frac{1}{(C_{cc}^{w})^{-1}})^{-1} = 27514$, with $p = 1, 2$. However, the Q-factor defined as $\Delta\omega/\omega_0$, with $\Delta\omega$ being the spectral bandwidth, was measured to be $Q_{m,p} = 27147$. The difference between these values is due to an extra term that determines the effective Q-factor of the cavities, which is the coefficient characterizing the losses due to the FC absorption in the cavities. The following expression represents the Q-factor calculated in a more accurate way:

$$Q_{e,p} \approx (\frac{1}{Q_p} + \frac{1}{(C_{cc}^{w})^{-1}} + \frac{1}{(J_{pp})^{-1}})^{-1}, \tag{22}$$

which can be used to calculate the Q-factor due to FCs, $Q_{FC,p} = 229630$. Thus, the value obtained for the effective Q-factor indicates that the energy in the cavities would have leaked out after $Q_{e,p}/f_p = 115.67\,\text{ps}$.

We now tune the input pulse at a wavelength of $\lambda_0 = 1278.3\,\text{nm}$, which is slightly different from that of the cavities, so that the interaction of the pulse with the cavities is maximum at the pulse carrier frequency. If we consider the the forward-propagating pulse, as per Fig. 3a), we can see that the peak power is reduced by more than 40% at the waveguide output due to various loss mechanisms, such as propagation loss and FCA, but also due to the coupling to the cavities. Part of this energy coupled to the cavities will decay via radiative processes and through FCA in the cavities. The remaining energy will couple back to the forward- and backward-propagating pulses. Indeed, it can be seen that there is a second peak reaching the output port, which must come from the cavities.

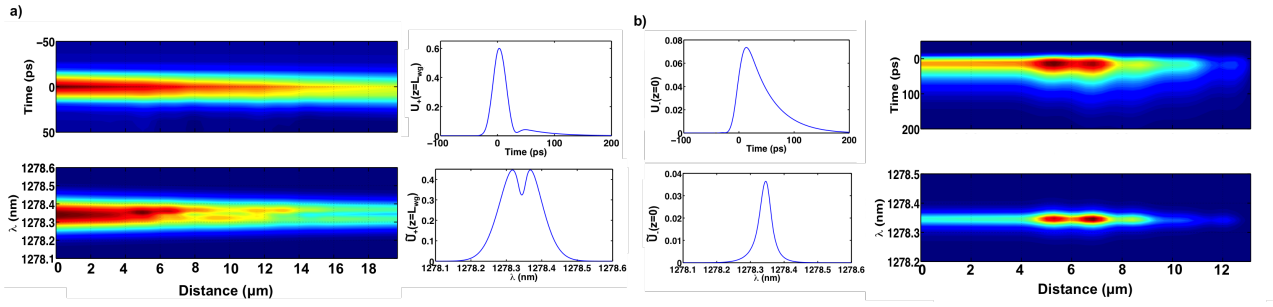

Figure 3. (a), (b) Evolution in the time and frequency domains of forward- and backward-propagating pulses, respectively. The right panels in (a) show the forward-propagating pulse at the output port, whereas the left panels in (b) show the backward-propagating pulse at the input port.

In the bottom panels of Fig. 3a), we show the evolution of the spectra along the z-direction, and it better illustrates where the effect of the cavities take place. The first one, which is centered at $L_{c_1} = 6.66\,\mu\text{m}$, distorts the forward pulse after $4\,\mu\text{m}$ and the second one at $L_{c_2} = 13.32\,\mu\text{m}$ clearly is responsible for the dip at the middle of the spectrum from around $14\,\mu\text{m}$. This is due to the fact that the optical fields of the cavities do extend few lattice constants around the center of the cavities. Note that the tilde symbol is used to denote the Fourier transform of the corresponding physical quantity.

Regarding the backward-propagating pulse, in the left panels in Fig. 3b) we present the backward-propagating pulse at the input of the waveguide, whose shape follows very closely the profile of the time dependence of the energy in the cavities. The spectra presented in the bottom panels show that the received pulse is located at the wavelength at which there is a dip in the spectrum of the transmitted pulse. In the right panels of the figure we can observe that the backward-propagating pulse starts to build up only at the locations of the cavities, and this is why the distance range is only represented up to L_{c_2}. One can also observe that the backward-propagating pulse reaches the largest power at the first cavity and then this power decreases towards the input port due to propagation losses and FCA.

With respect to the cavities, we illustrate in Figs. 4a) and 4b) the time variation of the normalized amplitude of the fields in cavity c_1 and c_2, respectively, the characteristic energy being $E_0 = 28.04\,\text{fJ}$. First, we note that the peak in the first cavity reaches a higher value than that in the second cavity, which is as expected since the forward-propagating pulse loses energy as it propagates along the waveguide. The inset between panels a) and b) is a zoom-in plot showing the superposition of the real part of both cavities field amplitudes, which oscillate at $f_{c_1} = f_{c_2} = 234.68\,\text{THz}$. Apart from the difference in amplitude just explained, there is also a difference in phase, which is mainly due to the phase variation the forward propagating pulse experiences from the first to the second cavity. Moreover, it can be seen the decay rate in both cavities fits well with the calculated effective Q-factor.

The plots in Figs. 5a) and 5b) show the FC distribution for the waveguide pulses and for the cavities, respectively. Regarding the FCs in the waveguide, the largest number is obviously at the input port where there is the largest peak power. From there, the FC density decreases along the z-direction due to the propagation loss and FC recombination processes. We can also observe the decay trend along z-direction is perturbed at about $5\,\mu\text{m}$, where the backward-propagating pulse reaches its highest power. Regarding the FC in the cavities, we can observe that, as expected, the FC density in the first cavity starts growing before that in the second cavity. Furthermore, the ratio between the maximum FC density in each cavity can be easily calculated by computing the following relation,

$$\frac{|U_{c_1,max}|^4}{|U_{c_2,max}|^4} = 1.6691, \tag{23}$$

which exactly matches the difference between the maximum number of FCs at each cavity, which is:

$$\frac{|U_{c_1,max}|^4}{|U_{c_2,max}|^4} = \frac{\bar{N}_{c_1,max}}{\bar{N}_{c_2,max}}. \tag{24}$$

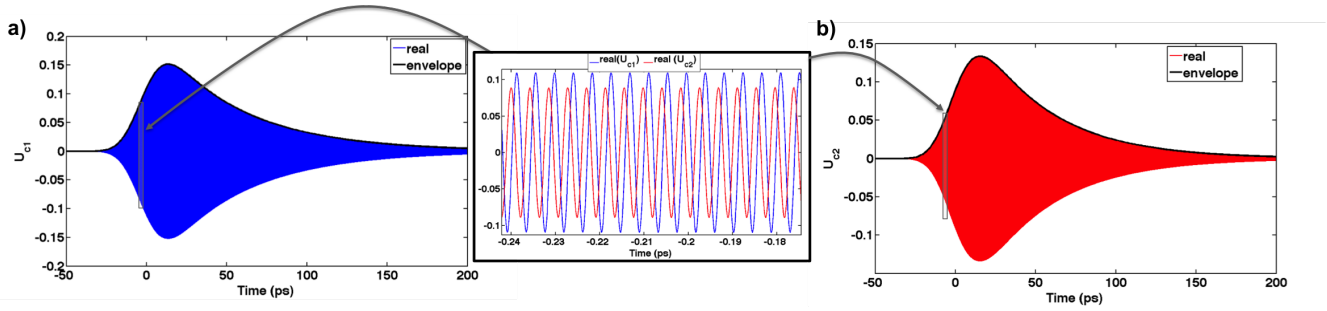

Figure 4. Time dependence of the real part of the normalized amplitudes U_{c_1} (a) and U_{c_2} (b), showing also the envelope in black. The inset between the two panels is a zoom-in plot of the real part of U_{c_1} (blue) and U_{c_2} (red).

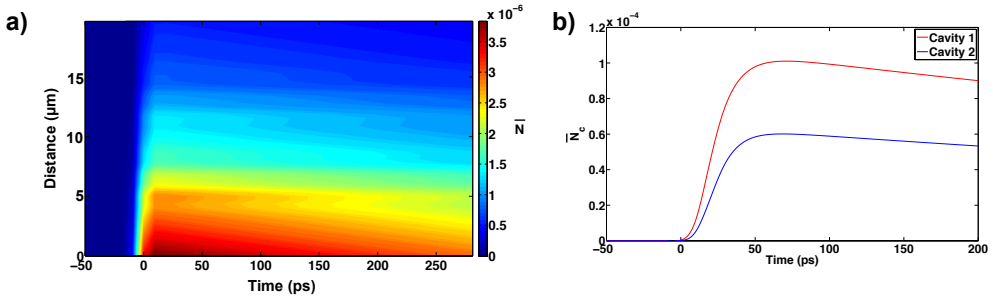

Figure 5. Free-carrier dynamics in the waveguide (a) and in the cavities (b). The densities shown are normalized to $N_0 = 7.343 \times 10^{24}\,\mathrm{m}^{-3}$.

The influence of the input pulse width on the system dynamics becomes relevant when it is comparable to the time it takes for most of the energy escape the cavities. By reducing the separation between cavities and waveguide by one row of holes, meaning $d_{cw} = 2a\sqrt{3}$, we obtain $C_{cc}^{w} = 1.5693 \cdot 10^{-4}$, for which the effective Q-factor of the cavities becomes $Q_{e,p} = 6028.3$. This can be translated into a characteristic time of 25.68 ps, needed for the energy in the cavity to radiate. Therefore, we assume that the pulse width varies from 2 ps to 30 ps. The results of these simulations are presented in Fig. 6, where we have plotted the time dependence of the forward- and backward-propagating pulses as well as that of the optical field in the cavities.

It can be observed that, when the pulse width T_0 is much smaller than the characteristic time associated to the effective Q-factor, the energy profile in the cavity shows the effect of forward- and backward-propagating pulses contributing to the energy level until the main waves have passed and then the remaining shape is the usual energy radiative decay associated to the Q-factor. This is no longer true when wider pulses are used since the optical pulses transfer energy into the cavities more slowly than the overall energy loss rate of these, so the effect of other waves of pulses interfering with the main pulse at the cavities is not noticeable. The most interesting pattern occurs for the backward-propagating pulse when $T_0 = 2$ ps. The two highest peaks correspond to the first reflected pulse from the first cavity and the first reflected pulse from the second cavity. The other peaks are built in a similar fashion but with the following reflected pulses. This explains the periodic nature of the remaining peaks. Moreover, it should be noted that, when $T_0 \ll Q_e/f_c$, the pulse shape in the transmitted port becomes more and more asymmetrical in time, whereas in the received port, the temporal pulse shape follows the back and forth waves pattern.

To conclude this section, we study the effect of varying the separation between the cavities on the optical response of the photonic structure. In particular, we seek the optimum separation that minimizes the amplitude

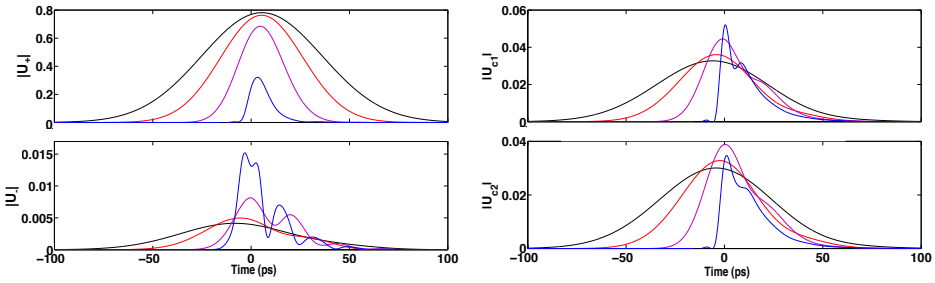

Figure 6. From top to bottom: effect of varying the pulse width on the forward-propagating pulse amplitude at the output port, the backward-propagating pulse amplitude at the input port, the amplitude of the energy function in the first cavity and the amplitude of the energy function in the second cavity, respectively. Black lines The pulse width was $T_0 = 30$ ps (black lines), $T_0 = 20$ ps (red lines), $T_0 = 10$ ps (purple lines), and $T_0 = 2$ ps (blue lines).

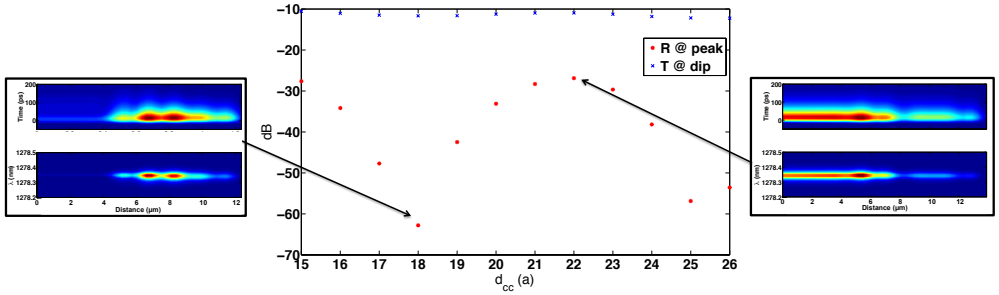

Figure 7. Effect of cavity-cavity separation d_{cc} on the transmitted (T) dip and reflected (R) peak levels in a case with $d_{cw} = 2.5\sqrt{3}a$, $T_0 = 10\,\text{ps}$ and $\lambda_0 = 1278.3\,\text{nm}$. The insets show the backward-propagating pulse dynamics for the lowest level measured at the input port (left) and for the maximum level measured at the output port (right).

of the reflected signal at the input port. A simple estimation of this optimum separation can be made by just ensuring the combination of phases from the main reflected waves arriving at the input port add to an odd number of π, this is:

$$2\beta_+ L_{c_1} = 2\beta_+ L_{c_1} + 2\beta_+ d_{cc} \pm n\pi, \tag{25}$$

with L_{c_1} the distance to the first cavity, L_{c_2} the distance to the second cavity, $d_{cc} = L_{c_2} - L_{c_1}$, and $n = 1, 3, 5, \ldots$. Since we want to maintain the input and output waveguide lengths we have been using so far, we can establish $L_{c_1} = 20a$, and model the distance between cavities by an integer number of lattice constants, $d_{cc} = ka$, so that Eq. (25) becomes:

$$2\beta_+ ka \pm n\pi = 0. \tag{26}$$

Given this relation, for $a = 333\,\text{nm}$, $\lambda_0 = 1278.3\,\text{nm}$ and $\beta_+ = 8.1993 \times 10^6\,\text{m}^{-1}$, we find that the value of k closest to an integer number is $k = 18.9852$ for $n = 33$. Based on this result, we perform several simulations with the cavity-waveguide separation fixed to four rows, but varying the cavity-cavity separation around the initial value of $d_{cc} = 20a$, namely from $d_{cc} = 15a$ to $d_{cc} = 26a$. We did not decrease any further the lower limit in order to maintain the cavities uncoupled from each other, and we did not consider larger separation distance because we wanted to keep the structure as compact as possible. In Fig. 7 we show the variation with d_{cc} of the transmitted dip and reflected peak values. Regarding the curve corresponding to the reflected pulse, the lowest level at the input port is achieved for $d_{cc} = 18a$, closely matching our estimated value. With respect to the transmitted curve, the dip level is fairly flat within the simulated range. Finally, the insets next to the main figure contain the time and frequency dynamics for the backward-propagating pulse in the case where the reflected pulse level at the input port is minimized (left) and where it is maximized (right), clearly showing the difference between destructive and constructive interference at the input port.

4. CONCLUSION

In summary, we have presented a novel, comprehensive, and rigorous mathematical model describing the pulsed dynamics in cavity-waveguide photonic nanostructures. Our model incorporates linear and nonlinear effects, including GVD, SPM, TPA, FC dispersion, and FCA. Both the mathematical model and the computational implementation have been described in detail and the resulting simulation framework has been applied to a silicon photonic crystal system consisting of a two high-Q cavities placed alongside a waveguide where a slow-light mode propagates. Our model predicts this system can potentially be used as a drop-filter, but we have illustrated that special attention must be paid on the influence of different design parameters on the optical response of the nanostructure as they can strongly impact on the pulsed dynamics and, thus, on the overall behavior of the device.

ACKNOWLEDGMENTS

This work has been sponsored by Airbus Defence and Space, Gunnels Wood Road, Stevenage SG1 2AS, United Kingdom.

REFERENCES

[1] Miller, D., "Rationale and challenges for optical interconnects to electronic chips", *Proc. IEEE* **88**, 728 (2000).

[2] Shacham, A., Bergman, K., and Carloni, L. P., "Photonic networks-on-chip for future generations of chip multiprocessors," *IEEE Trans. Comput.* **57**, 1246 (2008).

[3] Levy, J. S., Gondarenko, A., Foster, M. A., Turner-Foster, A. C., Gaeta, A. L., and Lipson, M., "Cmos-compatible multiple-wavelength oscillator for on-chip optical interconnects," *Nat. Photonics* **4**, 37 (2010).

[4] Soref, R., "The past, present, and future of silicon photonics," *IEEE J. Sel. Top. Quantum Electron.* **12**, 1678 (2006).

[5] Almeida, V. R., Barrios, C. A., Panepucci, R. R., and Lipson, M., "All-optical control of light on a silicon chip," *Nature* **431**, 1081 (2004).

[6] Panoiu, N. C., Bahl, M., and Osgood, R. M., "All-optical tunability of a nonlinear photonic crystal channel drop filter," *Opt. Express* **12**, 1605–1610 (Apr 2004).

[7] Akahane, Y., Asano, T., Song, B., and Noda, S., "High-Q photonic nanocavity in a two-dimensional photonic crystal," *Nature* **425**, 944 (2003).

[8] Joannopoulos, J., Johnson, S., Winn, J., and Meade, R., [*Photonic Crystals: Molding the Flow of Light, 2nd edition*], Princeton University Press, Princeton, 190-228 (2008).

[9] Mekis, A., Chen, J. C., Kurland, I., Fan, S., Villeneuve, P. R., and Joannopoulos, J. D., "High transmission through sharp bends in photonic crystal waveguides," *Phys. Rev. Lett.* **77**, 3787 (1996).

[10] Noda, S., Tomoda, K., Yamamoto, N., and Chutinan, A., "Full three-dimensional photonic bandgap crystals at near-infrared wavelengths," *Science* **289**(5479), 604-606 (2000).

[11] Panoiu, N. C., Bahl, M. and Osgood, R. M., "Optically tunable superprism effect in nonlinear photonic crystals," *Opt. Lett.* **28**, 2503-2505 (2003).

[12] Panoiu, N. C., Bahl, M. and Osgood, R. M., "Ultrafast optical tuning of a superprism effect in nonlinear photonic crystals," *J. Opt. Soc. Am. B* **21**, 1500-1508 (2004).

[13] Li, J., White, T. P., O'Faolain, L., Gomez-Iglesias, A., and Krauss, T. F., "Systematic design of flat band slow light in photonic crystal waveguides," *Opt. Express* **16**(9), 6227-6232 (2008).

[14] Krauss, T. F., "Slow light in photonic crystal waveguides," *Journal of Physics D: Applied Physics* **40**, 2666 (2007).

[15] Notomi, M., Kuramochi, E., and Tanabe, T., "Large-scale arrays of ultrahigh-Q coupled nanocavities," *Nat. Photonics* **2**, 741–747 (2008).

[16] Soljacic, M., Johnson, S. G., Fan, S., Ibanescu, M., Ippen, E., and Joannopoulos, J. D., "Photonic-crystal slow-light enhancement of nonlinear phase sensitivity," *J. Opt. Soc. Am. B* **19**, 2052-2059 (2002).

[17] McMillan, J. F., Yang, X., Panoiu, N. C., Osgood, R. M., and Wong, C. W., "Enhanced stimulated Raman scattering in slow-light photonic crystal waveguides," *Opt. Lett.* **31**, 1235-1237 (2006).

[18] Baba, T., "Slow light in photonic crystals," *Nat. Photonics* **2**, 465-473 (2008).

[19] Vlasov, Y. A., O'Boyle, M., Hamann, H. F., and McNab1, S. J., "Active control of slow light on a chip with photonic crystal waveguides," *Nature* **438**, 65-69 (2005).

[20] Corcoran, B., Monat, C., Grillet, C., Moss, D. J., Eggleton, B. J., White, T. P., O'Faolain, L., and Krauss, T. F., "Green light emission in silicon through slow-light enhanced third-harmonic generation in photonic-crystal waveguides," *Nat. Photonics* **3**, 206-210 (2009).

[21] Johnson, S. G. and Joannopoulos, J. D., "Block-iterative frequency-domain methods for Maxwell's equations in a planewave basis", *Opt. Express* **8**, 173 (2001).

[22] Group, R. D., "Bandsolve photonics software", www.rsoftdesign.com.

[23] Oskooi, A., Roundy, D., Ibanescu, M., Bermel, P., Joannopoulos, J., and Johnson, S., "Meep: A flexible free-software package for electromagnetic simulations by the fdtd method," *Comput. Phys. Commun.* **181**, 687-702 (2010).

[24] Ren, Q., You, J. W., and Panoiu, N. C., "Giant enhancement of the effective Raman susceptibility in metasurfaces made of silicon photonic crystal nanocavities," *Opt. Express* **26**, 30383-30392 (2018).

[25] Chen, X., Panoiu, N. C. and Osgood, R. M., "Theory of Raman-Mediated Pulsed Amplification in Silicon-Wire Waveguides," *IEEE J. Quantum Electron.* **42**, 160-170 (2006).

[26] Panoiu, N. C., McMillan, J. F. and Wong, C. W., "Theoretical Analysis of Pulse Dynamics in Silicon Photonic Crystal Wire Waveguides," *IEEE J. Sel. Top. Quantum Electron.* **16**, 257-266 (2010).

[27] Lavdas, S. and Panoiu, N. C., "Theory of pulsed four-wave mixing in one-dimensional silicon photonic crystal slab waveguides," *Phys. Rev. B* **93**, 115435 (2016).

[28] Osgood, R. M., Panoiu, N. C., Dadap, J. I., Liu, X., Chen, X., Hsieh, I-W., Dulkeith, E., Green, W. M. J. and Vlasov, Y. A., "Engineering nonlinearities in nanoscale optical systems: physics and applications in dispersion-engineered silicon nanophotonic wires," *Adv. Opt. Photon.* **1**, 162-235 (2009).

[29] Liang, T., Nunes, L., Sakamoto, T., Sasagawa, K., Kawanishi, T., Tsuchiya, M., Priem, G., Thourhout, D. V., Dumon, P., Baets, R., and Tsang, H., "Ultrafast all-optical switching by cross-absorption modulation in silicon wire waveguides," *Opt. Express* **13**, 7298-7303 (Sep 2005).

[30] Press, W. H., Teukolsky, S. A., Vetterling, W. T., and Flannery, B. P., [*Numerical recipes in C: The art of scientific computing, 2nd Edition*], Cambridge University Press, Cambridge, 379-383 (1992).

[31] Anderson, E., Bai, Z., Dongarra, J., Greenbaum, A., McKenney, A., Du Croz, J., Hammarling, S., Demmel, J., Bischof, C., and Sorensen, D., "Lapack: A portable linear algebra library for high-performance computers," *Supercomputing '90*, 2-11, IEEE Computer Society Press, Los Alamitos, CA, USA (1990).